Journal of Solid State Chemistry **160,** 167–173 (2001)
doi:10.1006/jssc.2001.9214, available online at http://www.idealibrary.com on IDEAL®

Observation of Antiferromagnetism in Marokite $CaMn_2O_4$

Christopher D. Ling[1]

Materials Science Division, Argonne National Laboratory, Argonne, Illinois 60439
E-mail: cling@anl.gov

J. J. Neumeier

Department of Physics, Florida Atlantic University, Boca Raton, Florida 33431

and

Dimitri N. Argyriou

Materials Science Division, Argonne National Laboratory, Argonne, Illinois 60439

Received February 26, 2001; accepted April 12, 2001; published online June 15, 2001

Marokite ($CaMn_2O_4$) has been identified as a low-level impurity in the solid-state synthesis of $Ca_{1-x}La_xMnO_3$ perovskites in the low-x region. In order to properly isolate the complex magnetic behavior of these important perovskites, the low-temperature magnetic structure and properties of marokite are determined and reported. All Mn ions are in the high-spin 3+ oxidation state. Jahn–Teller-distorted MnO_6 octahedra share both edges and vertices in a three-dimensional network, through which various exchange mechanisms cooperatively give rise to antiferromagnetic Mn^{3+} spin order. The magnetic order is evidenced below $T_N = 220$ K by a peak in the magnetic susceptibility and the appearance of symmetry-lowering magnetic Bragg reflections in neutron diffraction. © 2001 Academic Press

Key Words: **marokite; $CaMn_2O_4$; $Ca_{1-x}La_xMnO_3$; neutron powder diffraction; magnetic structure; magnetic susceptibility.**

I. INTRODUCTION

A prerequisite for the correct interpretation of powder diffraction data is a knowledge of any crystalline impurity phases present in a powder sample. This is especially important when a small number of characteristic reflections are involved, e.g., in modulated or magnetically ordered structures. In the course of an ongoing investigation into the magnetic behavior of La-doped $CaMnO_3$ perovskites (1), we identified marokite ($CaMn_2O_4$) as a minor (~ 1 wt%) impurity in the solid-state synthetic process. The significance of this small impurity was greatly magnified by the appearance of magnetic superstructure reflections at temperatures and d-spacings similar to those of the majority phase under investigation. This raised further concerns about possible effects of a small marokite impurity on magnetic susceptibility and magnetisation data collected using the same powder samples. In order to properly isolate the complex magnetic behavior of these important perovskites, therefore, we have undertaken a study of the low-temperature magnetic structure and properties of marokite.

II. EXPERIMENTAL

A specimen of $CaMn_2O_4$ was synthesised by mixing stoichiometric amounts of $CaCO_3$ and MnO_2 with a mortar and pestle for 10 min followed by reaction for 20 h at 1100°C. The sample was reground for 10 min and reacted at 1200°C. Three subsequent regrindings and 20-h reactions at 1300°C were conducted. After the final two regrindings the specimen was pressed into pellet form. This specimen was studied with neutron and X-ray diffraction, which indicated approximately 5 wt% $CaMnO_3$ as an impurity phase and is referred to as specimen A. A second sample (specimen B) was synthesised in a similar fashion with three additional regrinding and reaction steps to promote better homogeneity. This sample was reacted to a maximum temperature of 1250°C and was found to contain only approximately 1 wt% $CaMnO_3$ impurity.

Temperature-dependant time-of-flight (TOF) neutron powder diffraction data were collected between 20 and 300 K for specimen B on the Special Environment Powder Diffractometer (SEPD) at Argonne National Laboratory's Intense Pulsed Neutron Source (IPNS). Data were analyzed

[1] To whom correspondence should be addressed. Fax: 630-252-7777.

0022-4596/01 $35.00

using the program GSAS (2). Magnetic susceptibility measurements were conducted at 2000 Oe using a commercially available SQUID magnetometer.

III. RESULTS AND DISCUSSION

III.1. Magnetic Properties

The molar magnetic susceptibility χ is plotted in Fig. 1 vs temperature for specimen B. The susceptibility of specimens A and B were nearly identical, except for a slight ferromagnetic (FM) feature in the data of specimen A between 50 and 100 K due to the $CaMnO_3$ impurity. The upturn in χ below 50 K is likely the result of a minor paramagnetic Mn-based impurity phase at the level of a few percent. At $T_N = 220$ K a paramagnetic-to antiferromagnetic (AFM) phase transition is observed in the data. Analysis of the paramagnetic susceptibility above 300 K was conducted with the Curie–Weiss equation $\chi = C/(T + \Theta)$, where C is the Curie–Weiss constant and Θ is the Curie–Weiss temperature. Values of $C = 3.32(5)\,cm^3$-K/mole-Mn and $\Theta = 456(10)$ K were obtained. The Curie–Weiss constant, under the assumptions that the Landé g-factor is equal to 2 and the orbital angular momentum is quenched, yields a value of $S = 2.12(2)$ for the spin angular momentum. These results are consistent with Mn^{3+} in a high-spin $S = 2$ state, where S is the spin angular momentum. The positive value of Θ is consistent with the observation of AFM. In the inset of Fig. 1, the magnetization M is plotted versus magnetic field at 5 K. The linear behavior of M is consistent with AFM behavior and reveals no indication of the FM response typical for $CaMnO_3$ (1).

III.2. Magnetic Structure

The room-temperature crystal structure of natural marokite (3) was Rietveld-refined using room-temperature SEPD data. The results are presented in Table 1. Atomic displacement parameters were refined anisotropically for all sites, and ORTEP plots (99% probability) of the coordination environments of Mn and Ca are shown in Fig. 2. MnO_6 octahedra are highly Jahn–Teller (J–T) distorted, as expected for Mn^{3+} ions in a high-spin state. Empirically calculated atomic valences (4), reported in Table 1, show the environments of all atoms in the structure to be reasonable.

The refinement was repeated using low-temperature SEPD data. The magnetic structure was determined to be fully AFM between nearest-neighbor Mn^{3+} sites, requiring a doubling of the crystallographic unit cell along the short a axis. Spins were found to be oriented along the short a axis. No FM component was found, in agreement with magnetization data described above. The evolution of the refined magnetic moment with temperature is shown in Fig. 3, indicating a Néel temperature $T_N = 220(10)$ K, in agreement with magnetic susceptibility data described above. The refined moment at 20 K, $\mu_x = 3.792(18)\,\mu_B$/Mn, represents 94.8(5)% of the total expected spin-only ordered moment on Mn^{3+}. No evidence of a change of slope of the lattice parameters or volume near T_N due to the magnetic phase transition is evident within the resolution of the data (inset to Fig. 3).

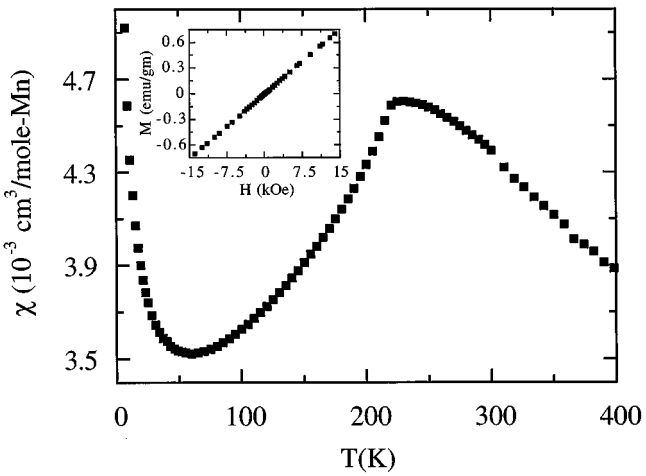

FIG. 1. Magnetic susceptibility χ in an applied magnetic field of 2000 Oe plotted vs temperature for $CaMn_2O_4$ (specimen B). The rapid reduction of χ below 220 K occurs as a result of AFM order. In the inset, the magnetization is plotted vs magnetic field at 5 K.

The results of the final refinement at 20 K are shown in Table 2, and the final fit to observed data is shown in Fig. 4. Note that in the final refinement, atomic displacement parameters were refined isotropically in order to reduce the number of variables while refining the magnetic structure. In Fig. 4, the strongest peak due to a small (~ 1 wt%) $CaMnO_3$ impurity is visible at $d = 2.16$ Å; inclusion of structural and magnetic reflections due to this impurity was

TABLE 1
Crystal Structure Data for $CaMn_2O_4$ from SEPD Neutron Powder Data at 300 K

	x (a)	y (b)	z (c)	Valence[a]	$100U_{11}$ (Å^2)
Ca	0.6813(14)	0.3523(5)	$\frac{1}{4}$	2.309	0.61(19)
Mn	0.2077(12)	0.1118(3)	0.0684(4)	2.930	0.76(16)
O1	0.5893(10)	$\frac{1}{4}$	0	1.808	0.79(17)
O2	0.1916(12)	0.1840(3)	$\frac{1}{4}$	2.159	0.88(19)
O3	0.1991(8)	0.4731(2)	0.1079(2)	2.101	0.39(11)
	$100U_{22}$ (Å^2)	$100U_{33}$ (Å^2)	$100U_{12}$ (Å^2)	$100U_{13}$ (Å^2)	$100U_{23}$ (Å^2)
Ca	1.3(2)	0.9(2)	0.06(17)	0	0
Mn	0.01(14)	0.26(14)	0.0(13)	0.03(13)	− 0.08(10)
O1	0.24(16)	0.82(17)	0	0	0.09(14)
O2	0.57(16)	0.18(16)	0.05(13)	0	0
O3	0.41(11)	0.51(11)	0.19(9)	− 0.014(10)	0.03(8)

[a] Empirically calculated atomic valence (4).

Note. Pbcm (No. 57): $a = 3.15886(8)$, $b = 9.9958(2)$, $c = 9.6776(2)$ Å, $R_p = 0.0772$, $wR_p = 0.1255$, $R(F^2) = 0.0594$, $\chi^2 = 1.121$.

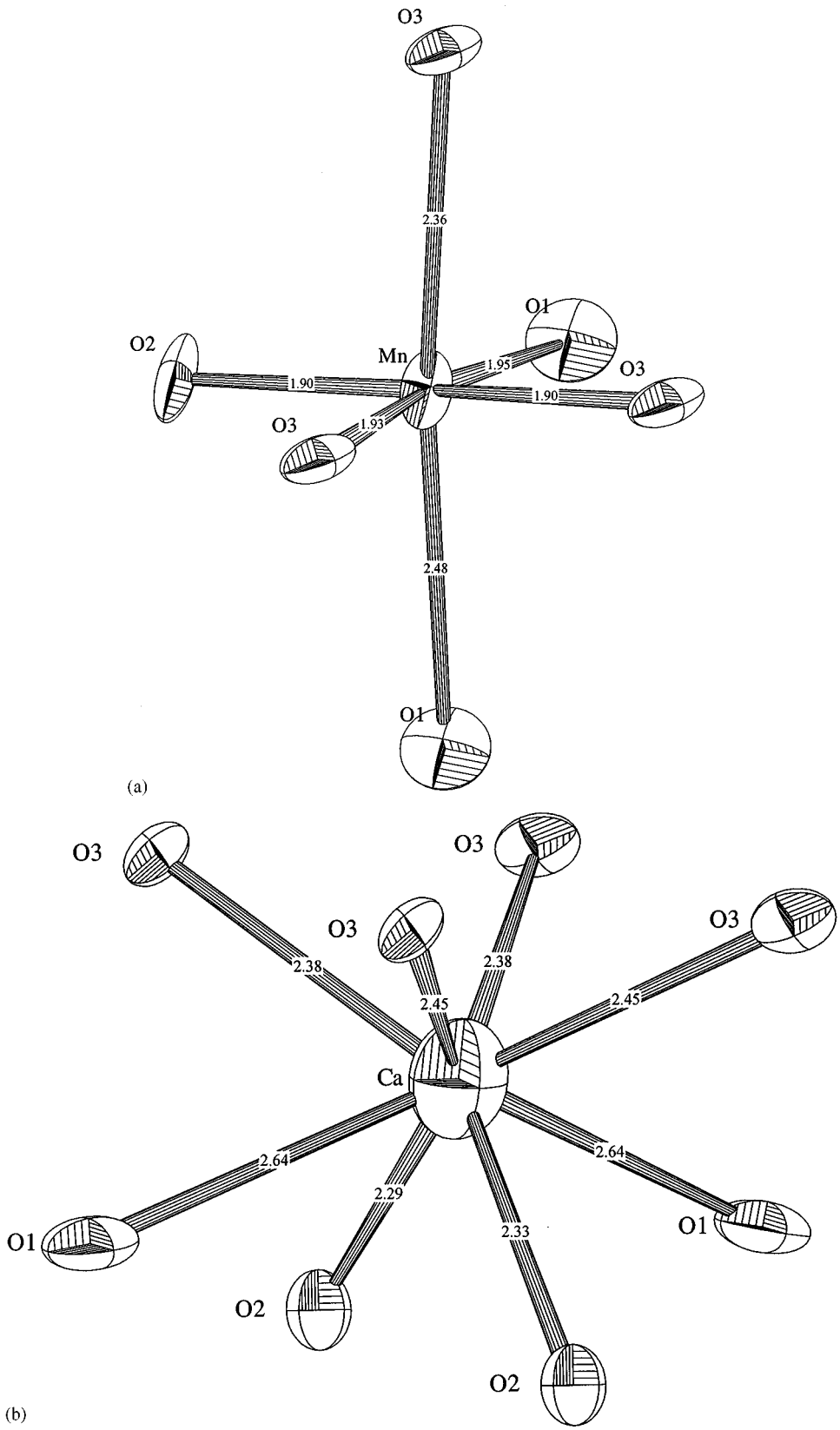

FIG. 2. ORTEP plots (99% probability) of the (a) MnO_6 octahedral and (b) CaO_8 polyhedral coordination environments in $CaMn_2O_4$ at 300 K. Bonds lengths are labeled (Å).

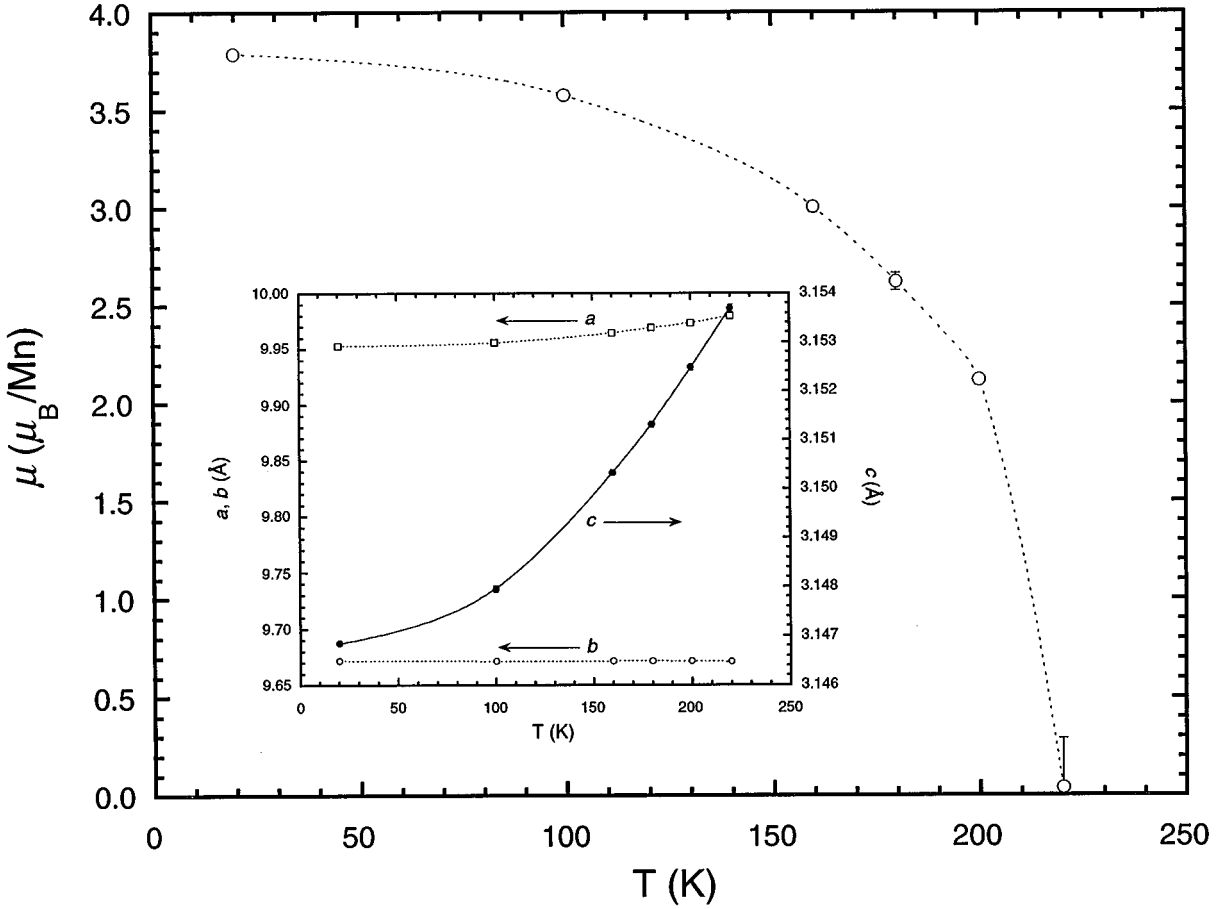

FIG. 3. Temperature dependence of the AFM long-range-ordered moment of $CaMn_2O_4$, obtained by Rietveld refinement of neutron powder diffraction data. The inset shows the temperature dependence of the lattice parameters. Error bars are smaller than symbols.

not found to significantly affect the results, and was therefore not included in the final refinement. Strong magnetic reflections (top row of reflection markers) due to the AFM superstructure can be seen at high *d*-spacings and are labeled in the inset to Fig. 4b.

The final refined crystal and magnetic structure at 20 K is shown in Fig. 5. CaO_8 polyhedra are coupled by triangular-face-sharing along the *x* direction and vertex-sharing along the *z* direction. MnO_6 octahedra are both vertex-sharing and edge-sharing, creating the complex Mn–O connectivity that is highlighted in Fig. 5c. The interactions giving rise to the AFM structure are now discussed in terms of the relationship between the Mn site (a) and its nearest neighbors (b through g), as labeled in Fig. 5c.

TABLE 2
Crystal Structure Data for $CaMn_2O_4$ from SEPD Neutron Powder Data at 20 K

	x (*a*)	*y* (*b*)	*z* (*c*)	$100U_{iso}$ (Å^2)
Ca	0.6854(7)	0.35197(19)	$\frac{1}{4}$	0.76(4)
Mn	0.2052(6)	0.11245(17)	0.06841(17)	0.10(3)
O1	0.5969(5)	$\frac{1}{4}$	0	0.44(4)
O2	0.1944(6)	0.18431(16)	$\frac{1}{4}$	0.36(3)
O3	0.2001(4)	0.47309(12)	0.10835(11)	0.31(2)

Note. $a = 3.14685(5)$, $b = 9.95280(13)$, $c = 9.67166(13)$ Å, $\mu_x = 3.792(18)$ μ_B/Mn, $R_p = 0.0419$, $wR_p = 0.0670$, $R(F^2) = 0.0374$, $\chi^2 = 1.512$.

Given the magnitude of the J–T distortion ($\sim 25\%$ elongation of the axial relative to the equatorial Mn–O distances), we can assume all the e_g electron density of Mn^{3+} to reside in d_{z^2}-type orbitals, oriented along the bonds drawn in darker gray in Fig. 5c. We can then use Goodenough's qualitative rules of semicovalent exchange (5) to interpret the magnetic interactions. Along the $\sim 180^\circ$ Mn(a)–O–Mn(g) bonding path, a filled d_{z^2}-type orbital on Mn(g) and an unfilled $d_{z^2y^2}$-type orbital on Mn(a) overlap a $p\sigma$ orbital on the oxygen atom; this interaction is expected to be FM (analogous to double exchange), as observed. The relationships between Mn(a) and Mn(b, d, and e) all involve two $\sim 90^\circ$ Mn–O–Mn bonds, in which case the role of the anion is generally subsidiary to direct (AFM) exchange

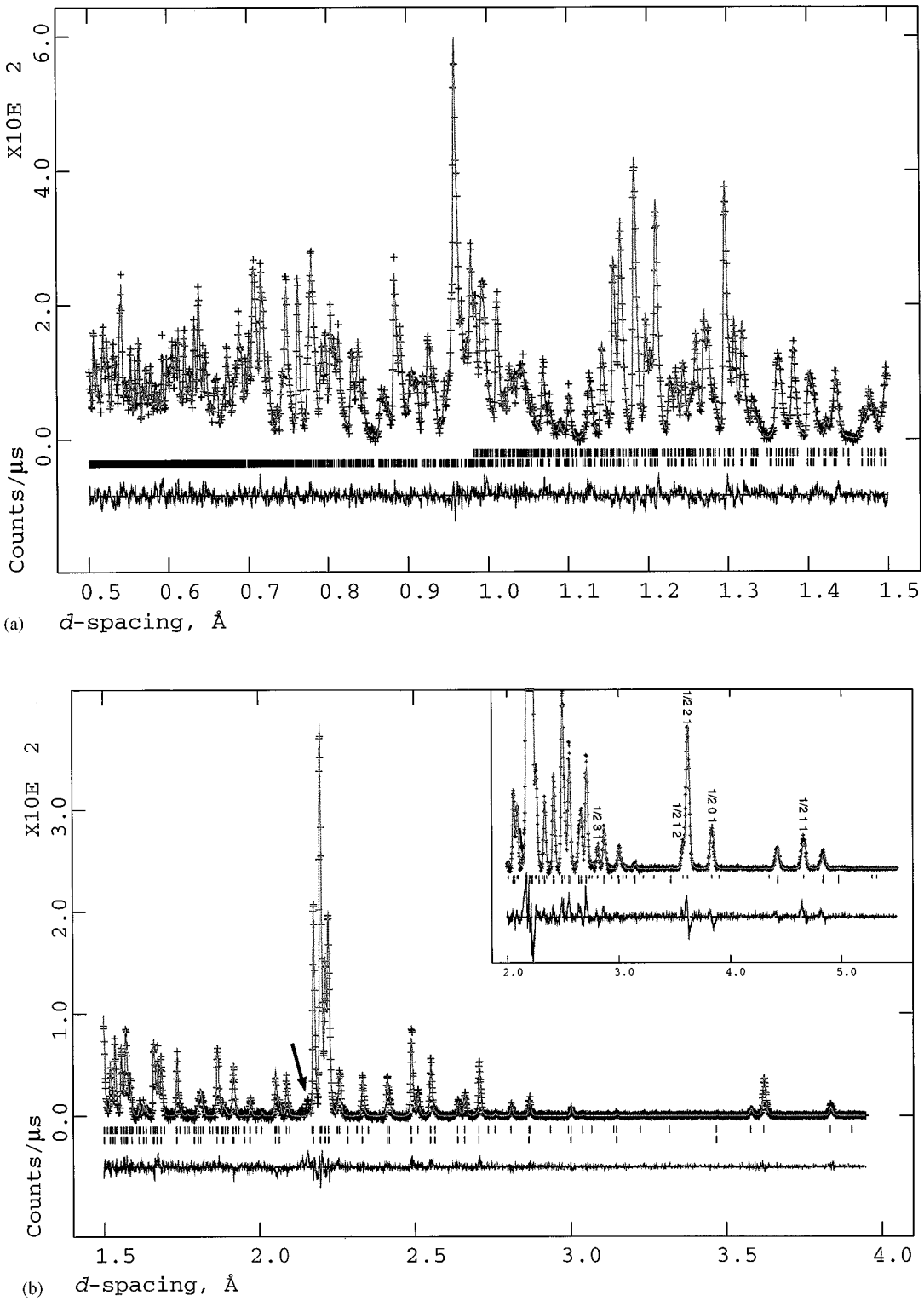

FIG. 4. Final observed, calculated (solid line), and difference neutron powder diffraction profile for $CaMn_2O_4$ (specimen B). Data collected on the backscattering detector bank of SEPD at 20 K. The top row of reflection markers refers to the magnetic phase. The arrow indicate the strongest peak due to a small ($\sim$ 1 wt%) $CaMnO_3$ impurity. The inset to (b) shows data collected on the 60° bank and highlights strong magnetic reflections.

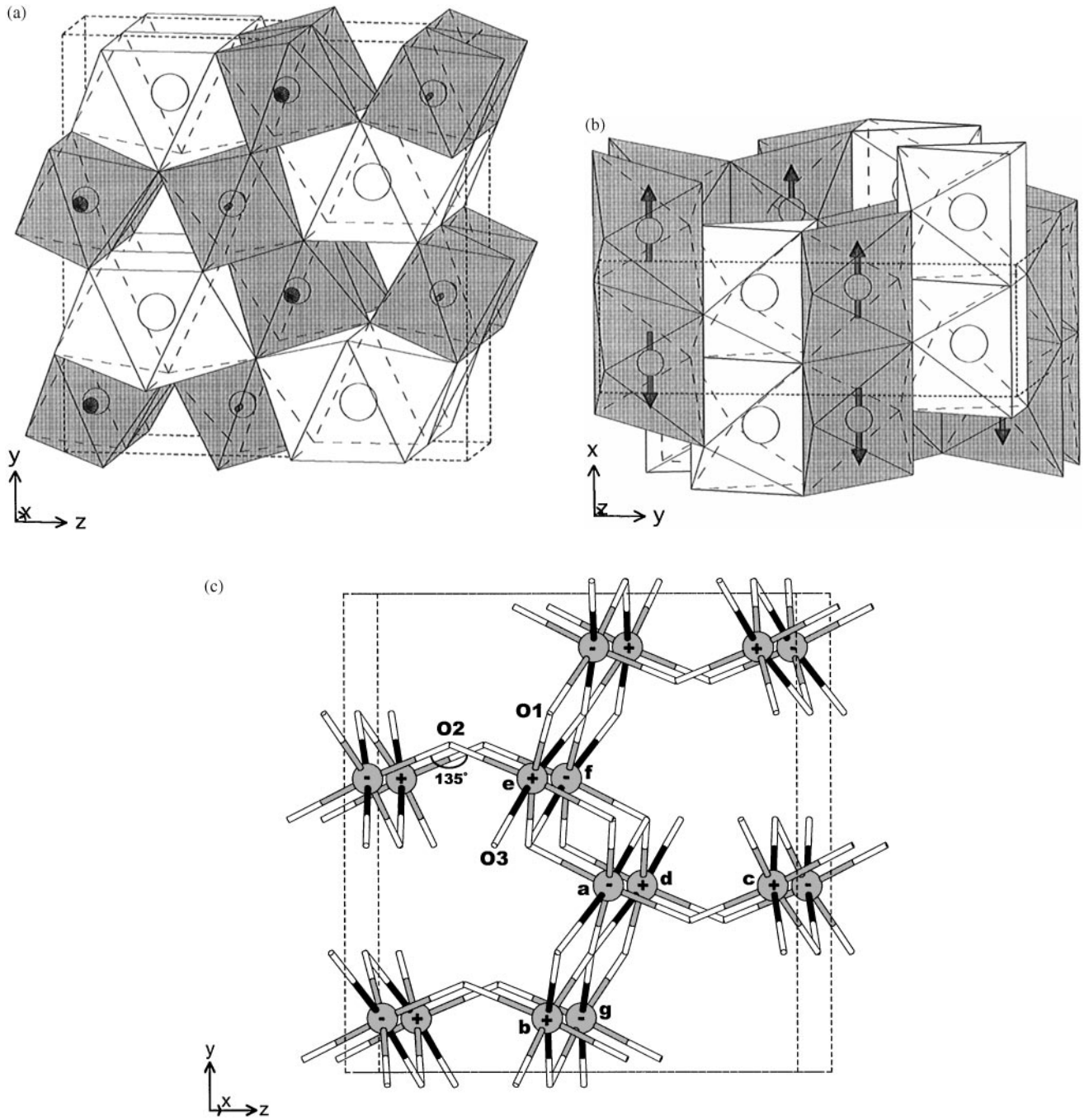

FIG. 5. (a, b) Final refined structure of $CaMn_2O_4$ at 20 K, showing complete MnO_6 (gray) and CaO_8 (white) polyhedra within the range ($-1 < x < 2$, $-0.1 < y < 1.1$, $-0.2 < z < 1.2$). The orientations of refined moments on Mn sites are shown as arrows. (c) The connectivity of complete MnO_6 octahedra within the range ($-1 < x < 2$, $-0.1 < y < 1.1$, $-0.2 < z < 1.2$) is shown. The orientations of refined moments on Mn sites (along x) are indicated by $+/-$ symbols. Elongated Mn–O bonds due to J–T distortions are indicated by darker gray shading. The three unique oxygen sites and the only significantly non $-90°$ Mn–O–Mn angle are labeled. Magnetic interactions between labeled Mn sites (a–g) are discussed in the text.

interactions between t_{2g} orbitals on Mn sites. Additional superexchange interactions where d_{z^2}-type orbitals act through oxygen p orbitals are of the types summarized in Fig. 43 of Goodenough (5) (Mn(a)–Mn(b), Cases 1 + 2; Mn(a)–Mn(d), Cases 3 + 3; Mn(a)–Mn(e), Cases 2 + 2); in all cases the net interaction is predicted to be AFM as observed. The interaction between Mn(a) and Mn(f) is also expected to be AFM (same case as Mn(a)–Mn(d)); however, it is clearly observed to be FM. This sole unfavorable magnetic interaction experienced by Mn(a) is of the weakest

type (the superexchange component is in fact FM (5)), and is in competition with the four favorable ones already described. The observation of almost complete (94.8(5)%) spin order indicates that this competition is resolved as expected without any significant residual spin frustration. The final interaction, between Mn(a) and Mn(c), takes place through a 135° Mn–O–Mn bond. This angle lies in the transition zone between FM (angles close to 180°) and AFM (angles close to 90°) superexchange interactions, and consequently the interaction is difficult to predict and expected to be weak. The high degree of (AFM) order observed reflects the fact that this interaction is entirely cooperative and has no competition.

IV. SUMMARY

Low-temperature magnetic susceptibility, magnetization, and neutron powder diffraction data for marokite $CaMn_2O_4$ have been presented and interpreted. The phase is AFM below $T_N = 220$ K, giving rise to a peak in the susceptibility and magnetic Bragg peaks (*a*-axis doubled) in the neutron diffraction. These data and results should make it easier to identify $CaMn_2O_4$ as an impurity and account for its presence both structurally and magnetically. In addition, $CaMn_2O_4$ itself presents an interesting and novel AFM structure that can be understood in terms of simple quantitative exchange interactions.

ACKNOWLEDGMENTS

This work was supported by the National Science Foundation under CAREER grant DMR 9982834 (J.J.N.) and by the U.S. Department of Energy, Basic Energy Sciences–Materials Sciences, under Contract W-31-109-ENG-38 (C.D.L., D.N.A.).

REFERENCES

1. J. J. Neumeier and J. L. Cohn, *Phys. Rev. B* **61,** 14,319 (2000).
2. A. C. Larson and R. B. V. Dreele, "GSAS: General Structure Analysis System." Los Alamos National Laboratory, Los Alamos, NM, 1991.
3. M.-M. Couffon, G. Rocher, and J. Protas, *C. R. Hebd. Seances Acad. Sci.* **258,** 1847 (1964); G. Lepicard and J. Protas, *Bull. Soc. Fr. Mineral. Crystallogr.* **89,** 318 (1966).
4. N. E. Brese and M. O'Keeffe, *Acta Crystallogr. Sect. B* **47,** 192 (1991).
5. J. B. Goodenough, "Magnetism and the Chemical Bond." Wiley, Cambridge, MA, 1963.